

Article

N-Rich Algal Sludge Biochar for Peroxymonosulfate Activation toward Sulfadiazine Removal

Chao Liu ^{1,2,†}, Zhenxiang Chen ^{3,†}, Ruiqin Kang ¹, Jing Wang ¹, Qingwei Lu ¹, Tao Wang ¹, Dayong Tian ^{1,*}, Ying Xu ^{2,*}, Zhan Wang ⁴ and Huiping Ding ⁵

¹ College of Chemistry and Environmental Engineering, Anyang Institute of Technology, Anyang 455000, China

² College of Chemistry and Chemical Engineering, Henan University, Kaifeng 475004, China

³ Jiangsu Xingzhou Ecological Environment Technology Co., Ltd., Nanjing 210004, China

⁴ Beijing Key Laboratory for Green Catalysis and Separation, Department of Chemistry and Chemical Engineering, Beijing University of Technology, Beijing 100124, China

⁵ College of Chemistry and Chemical Engineering, Henan Chemical Technician College, Kaifeng 475002, China

* Correspondence: tiandayong@163.com (D.T.); hdxccxu@126.com (Y.X.)

† These authors contributed equally to this work.

Abstract: The fabrication of a green, high activity and low-cost carbon-based catalyst capable of activating new oxidant (peroxymonosulfate, PMS) for contaminants abatement is needed. In this research, we prepared novel N-doped biochars via one-step pyrolysis of algal sludge without external nitrogen sources. The obtained ASBC800 possessed the largest specific surface area ($S_{\text{BET}} = 145.596 \text{ m}^2 \text{ g}^{-1}$) and thus it displayed the best catalytic performance, as revealed by the effective elimination of sulfadiazine (SDZ, >95% within 70 min) with 0.2 g L^{-1} ASBC800 and 0.5 mM PMS. Both radical species (e.g., $\text{SO}_4^{\bullet-}$, and $\bullet\text{OH}$), and nonradical regime ($^1\text{O}_2$ and electron-transfer) contributed to SDZ oxidation, in which ASBC800 played essential roles in activating PMS, accumulating SDZ, and regulating electron shuttle from SDZ to ASBC800-PMS*. Overall, this work not only provides a novel strategy for the synthesis of N-rich and cost-effective biochar but also promotes the development and application of carbon-based functional materials in environmental remediation.

Keywords: peroxymonosulfate; pre-adsorption; oxidation; electron-transfer; N doping



Citation: Liu, C.; Chen, Z.; Kang, R.; Wang, J.; Lu, Q.; Wang, T.; Tian, D.; Xu, Y.; Wang, Z.; Ding, H. N-Rich Algal Sludge Biochar for Peroxymonosulfate Activation toward Sulfadiazine Removal. *Coatings* **2023**, *13*, 431. <https://doi.org/10.3390/coatings13020431>

Academic Editor: Ioannis V. Yentekakis

Received: 19 October 2022

Revised: 29 November 2022

Accepted: 1 December 2022

Published: 14 February 2023



Copyright: © 2023 by the authors. Licensee MDPI, Basel, Switzerland. This article is an open access article distributed under the terms and conditions of the Creative Commons Attribution (CC BY) license (<https://creativecommons.org/licenses/by/4.0/>).

1. Introduction

Recently, peroxymonosulfate-based advanced oxidation processes (PMS–AOPs) have received increasing attention for pollutants removal [1–3]. Various reactive oxygen species (ROS) can be produced in this oxidation process, including sulfate radical ($\text{SO}_4^{\bullet-}$), hydroxyl radical ($\bullet\text{OH}$) and singlet oxygen ($^1\text{O}_2$), which possess much higher redox potentials than their parent oxidants (PMS, 1.75–1.82 V) [4]. In addition, a novel mediated electron transfer regime may occur between target contaminants and oxidants without the generation of ROS [5–7].

In order to produce ROS, it is of great importance to break the O–O bond of the PMS. Metal-free carbon-based catalysts have recently aroused widespread attention owing to their environmental protection and easy preparation [8]. Carbonaceous materials (e.g., activated carbon [9], reduced graphene oxide [10], porous carbon [11], carbon nanotubes [12] and nanodiamonds [13]) have been proven to be potential green catalytic materials for PMS activation due to their abundant oxygen-containing functional groups, edge defects, and porous structures. In addition to the abovementioned carbon-based catalysts, biochar is deemed a promising candidate for catalysis [14]. Biochar is a black solid obtained via high-temperature pyrolysis and often used as an excellent adsorbent [15,16]. Compared with other catalytic materials such as metal-based catalysts (e.g., Co, Fe, Cu, Mn), biochar has the advantages of easy preparation, a wide variety of raw precursors and low cost [17,18]. However, the catalytic activity of pristine biochar is often unsatisfactory owing to its limited

S_{BET} and undeveloped pore structure. Thus, several modification methods (e.g., metal doping and heteroatomic doping) have been applied to enhance the catalytic performance of pristine biochar [19,20]. Among others, N doping has been deemed a popular tool to boost the catalytic activity of pristine biochar [21]. N doping can enhance the interaction between catalysts and oxidants through changing the electrical potential on the carbon surface [22]. Nevertheless, the addition of external nitrogen sources (urea, thiourea, melamine, NH_4NO_3 , NH_4Cl , $\text{NH}_3 \cdot \text{H}_2\text{O}$, etc.) is needed when preparing the N-doped biochar, which increases the preparation cost [21,23,24]. For instance, Wu et al. [23] prepared N-doped biochar by using pharmaceutical sludge and urea solid as the feedstocks, which may increase the preparation cost. Therefore, it is of great importance to develop N-doped biochars without exogenous nitrogen dopants, which may promote the development and application of biochars in environmental remediation. Interestingly, algae, as it contains a large amount of protein, can be directly transferred to N-doped biochars without using extra nitrogenous chemical reagents [25–27]. It was reported that N-abundant Taihu blue algae biomass could be used as the feedstock for N self-doping porous carbon preparation [28]. Thus, it could be speculated that the algal sludge obtained by the mechanical pressure filtration of algal slurries might be a promising precursor for N-doped biochars preparation. Notably, it is still a big challenge to effectively dispose of algal sludge and thus translating the algal sludge into valuable biochars may be an alternative solution. As one of the most widely used antimicrobial compounds in animal husbandry, relatively high sulfadiazine (SDZ) residues were detected in the environment [29]. Therefore, it is urgent that green and efficient methods for SDZ-contaminated water purification are developed.

Consequently, this study aimed to prepare N-rich biochars from algal sludge for PMS activation. The physicochemical properties of the N-doped biochars along with the adsorptive and oxidative degradation of SDZ were systematically investigated. Moreover, the activation mechanism of PMS by N-doped biochar was analyzed in detail. This study will provide a low-cost and efficient strategy for N-doped biochars preparation and establish an integrated oxidation process for SDZ-contaminated water cleanup.

2. Materials and Methods

2.1. Chemicals and Regents

SDZ (Table S1) and PMS were obtained from Aladdin, China. All other reagents were analytical grade (Text S1).

2.2. Preparation and Characterization of the ASBCx

The algal sludge was collected from a sewage plant in Wuxi, China. Firstly, the algal sludge was dried at 80 °C and then mechanically grinded and sieved to 0.15 mm. The obtained powdered sample was placed in an oven and heated to a required temperature (400, 500, 600 and 800 °C) at 5 °C min^{-1} and held for 2 h. The obtained black solids were then ground into fine powders and named as ASBCx, where x represented the annealing temperature (400, 500, 600 and 800 °C). Detailed information on various characterizations and electrochemical experiments is given in Text S2 and Text S3, respectively.

2.3. Adsorption Studies

Experiments on SDZ adsorption were performed in a 100 mL bottle containing 50 mL of SDZ solution (5 mg L^{-1}) and 0.2 g L^{-1} of ASBCx. The mixture was stirred at ambient temperature with a magnetic stirrer. At regular intervals (2, 5, 10, 20, 40, 60, 120 min), liquid samples were taken from the mixture and filtered with 0.2 mm of filter to remove the solid catalyst for analysis. Then, the adsorption behavior of SDZ on ASBCx was further studied by adsorption kinetics (Text S4).

2.4. Catalytic Degradation of SDZ

SDZ, as a model pollutant, was selected as a degradative substrate to evaluate the catalytic activity of ASBCx. The SDZ degradation was conducted in a glass beaker (100 mL) containing 50 mL of SDZ solution (5 mg L^{-1}). First, 10 mg of ASBCx was dispersed in a SDZ solution and stirred for 30 min to reach adsorption equilibrium. Then, 0.5 mM of oxidants were injected into the suspension to initiate catalytic reaction. At regular intervals (2, 5, 10, 20, 30, 40 min), 0.5 mL of solution was withdrawn, filtered with 0.2 mm of filter to remove the ASBCx, and quenched with 0.5 mL of methanol for analysis. More details of degradation experiments and analytical methods are provided in Text S5 and Text S6, respectively.

3. Results and Discussion

3.1. Characterizations

The SEM images of the biochars prepared under 400 and 800 °C are shown in Figure 1a,b, respectively. As depicted in Figure 1a, ASBC400 exhibited a massive and plane structure, which had a relatively smooth surface. In contrast, ASBC800 (Figure 1b) underwent a dramatic change and a large number of irregular defect structures appeared on the surface, which might be the active sites for pollutant adsorption. In addition, compared with the TEM image of ASBC400 (Figure 1c), it could be observed that plenty of nano-spaces/channels were formed in ASBC800 (Figure 1d), which was able to expose abundant active sites and beneficial for nanoconfinement effects, boosting the PMS activation and pollutants adsorption.

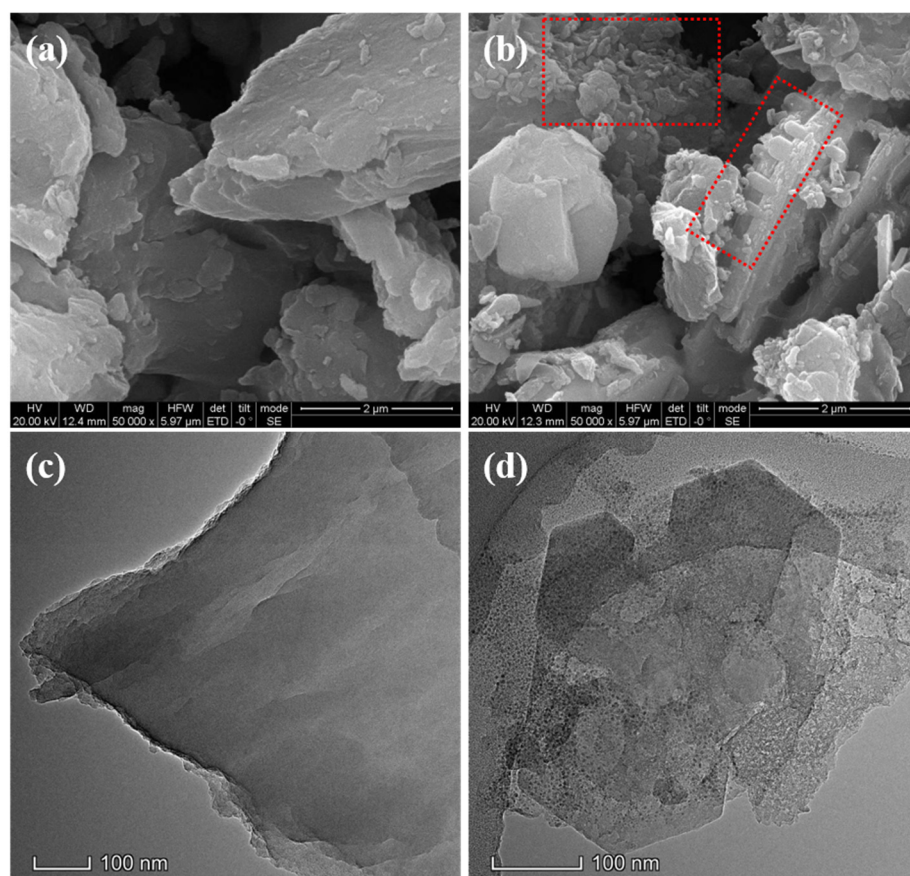


Figure 1. SEM images of ASBC400 (a), ASBC800 (b), and TEM images of ASBC400 (c) and ASBC800 (d).

As depicted in Figure 2, N_2 adsorption/desorption isotherms were characterized, which presented type IV, and the hysteresis loop occurred at the medium pressure end. These phenomena were due to N_2 condensation and accumulation in the porous channel, demonstrating that ASBCx were porous materials [21]. Moreover, the pore size distribution of ASBCx is listed in Table 1, which was mainly between 6 and 10 nm, and belonged to microporous and mesoporous. With the increase in pyrolysis temperature, the S_{BET} increased from 84.017 to 145.596 $m^2 g^{-1}$. Comparing the results, it could be seen that the higher pyrolysis temperature endowed ASBC800 with a larger S_{BET} . Thus, the ASBC800 with larger S_{BET} may have more active sites for pollutants and oxidants adsorption.

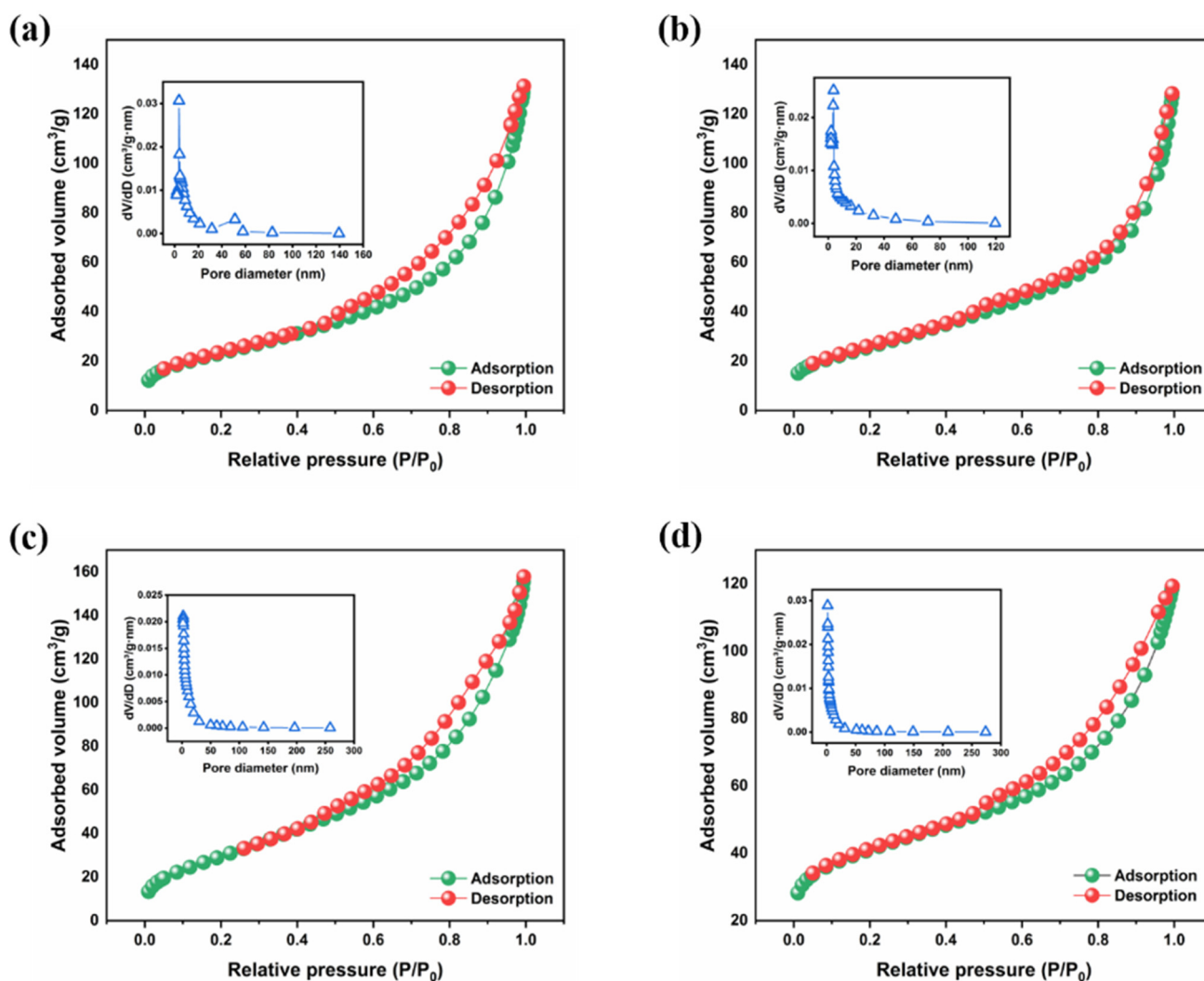


Figure 2. BET and pore size distribution of ASBC400 (a), ASBC500 (b), ASBC600 (c), and ASBC800 (d).

Table 1. Basic information of ASBCx.

Samples	S_{BET} ($m^2 g^{-1}$)	Pore Volume ($cm^3 g^{-1}$)	Average Pore Diameter (nm)
ASBC400	84.017	0.194	9.756
ASBC500	93.210	0.188	7.447
ASBC600	110.686	0.232	7.636
ASBC800	145.596	0.179	6.220

As depicted in Figure 3a, the Raman spectra of ASBCx showed two representative bands at $1343 cm^{-1}$ (D bands) and $1588 cm^{-1}$ (G bands), which originated from the defects and disorder of carbon atomic crystals and the graphitic structures, respectively. The

intensity ratios of D to G (I_D/I_G) clearly indicated the defective degree of the ASBCx [30]. Therefore, the higher I_D/I_G value of ASBC800 (0.972) than ASBC600 (0.969), ASBC500 (0.957), and ASBC400 (0.860) suggested higher defected carbon and it could be concluded that more new structural defects would be created under higher pyrolysis temperature. FTIR spectroscopy in the wavenumber range of 4000 to 500 cm^{-1} was conducted to investigate evolution of the surface of ASBCx. As displayed in Figure 3b, the band at 3428 cm^{-1} could be allotted to –OH stretching vibrations, whereas the peak at 2928 cm^{-1} was assigned to the C–H bond stretching vibrations [19]. Moreover, the peaks at 1470 cm^{-1} (C–C), 1592 cm^{-1} (C=C), and 1064 cm^{-1} (C–O) were identified [19]. Notably, the peak at 1174 cm^{-1} on ASBCx was owing to the formation of C–N bonds, which might be beneficial for oxygen reduction reaction (ORR) kinetics, boosting the ORR process [31]. In addition, the peak at 560 cm^{-1} was the Fe–O characteristic vibration mode of ASBCx [32]. XPS spectra (Figure 3c) confirmed ASBCx were composed of C, N, and O elements. Moreover, a signal appeared at 708.8 eV representing Fe 2p was observed in the XPS measurement spectra of ASBCx [33], which was due to the addition of iron-containing reagent in the process of algal sludge pressure filtration.

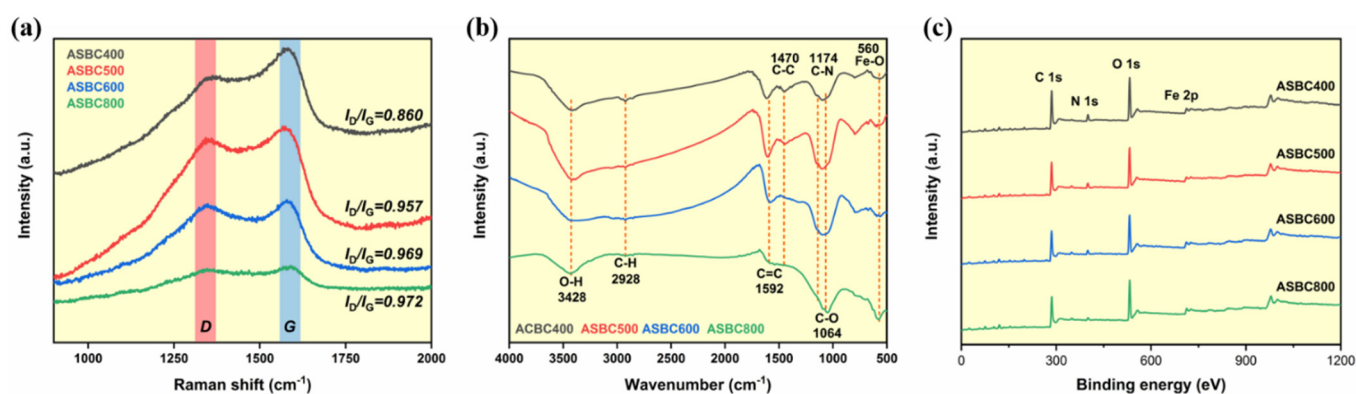


Figure 3. Raman spectra (a), FTIR spectra (b), and XPS spectra (c) of ASBCx.

The C 1s XPS spectra (Figure S1) were divided into four sections at: 284.6, 285.3, 286.4, and 533 eV, indicating C=C ($\text{sp}^2\text{-C}$), C–C ($\text{sp}^3\text{-C}$), C–O, and C=O, respectively. The O 1s spectra (Figure S2) were also divided into four sections: –C=O (531.4), –O–C=O (532.5), C–O (533.7), and H_2O (535.0). The Fe 2p core levels of ASBCx were analyzed, and Fe 2p was divided into two pairs of doublets and two satellite peaks (Figure S3). The peaks at 710.6 and 723.8 eV belonged to Fe^{2+} species, whereas the peaks at 713.6 and 726.8 eV belonged to Fe^{3+} species [34]. Additionally, the other two peaks at 717.2 and 732.8 eV originated from two satellites. The N 1s spectra of ASBCx were fitted into different components, including pyridinic N (N in 6-atom ring, 397.9 eV), pyrrolic N (N in 5-atom ring, 399.5 eV) and graphitic N (N in graphitic carbon plane, 401.1 eV). The content of the N configurations also exhibited correlation with the pyrolysis temperature (Figure 4). The percentage of graphitic N significantly increased from 15.62% to 34.82% when the pyrolysis temperature increased from 400 to 800 $^{\circ}\text{C}$. It was well accepted that the graphitic N could be more reactive in PMS activation than other N configurations [35,36]. Thus, the increased graphitic N in ASBC800 implied its best performance for PMS activation and contaminants removal.

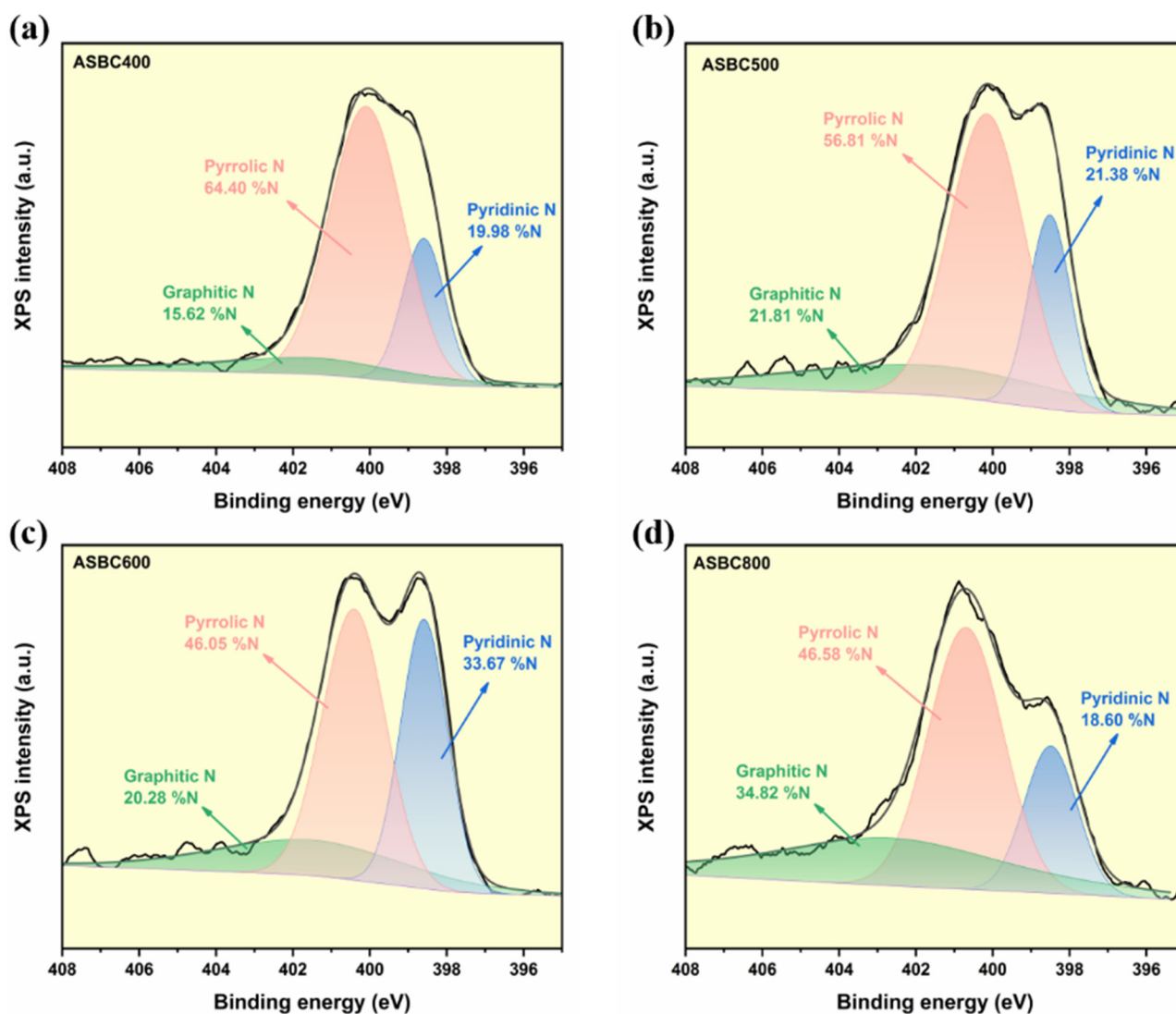


Figure 4. N 1s high-resolution spectrum of ASBC400 (a), ASBC500 (b), ASBC600 (c), and ASBC800 (d).

3.2. Adsorptive Experiment

As shown in Figure 5a,b, the SDZ molecule could be rapidly transferred to the ASBCx surface via adsorption. The better correlation coefficients (Table 2, $R^2 > 0.967$) were obtained by fitting with a pseudo-second-order kinetic model, indicating that chemisorption might dominate the adsorption process. More specifically, ASBC800 had the highest q_e value of 12.532 mg g^{-1} , followed with ASBC600 (1.175 mg g^{-1}), ASBC500 (0.993 mg g^{-1}), and ASBC400 (0.482 mg g^{-1}), suggesting the adsorption affinity of the catalyst could be boosted under a higher pyrolysis temperature. Additionally, as abovementioned in Table 1, the largest S_{BET} would be obtained under $800 \text{ }^\circ\text{C}$, which would be beneficial for contaminant adsorption.

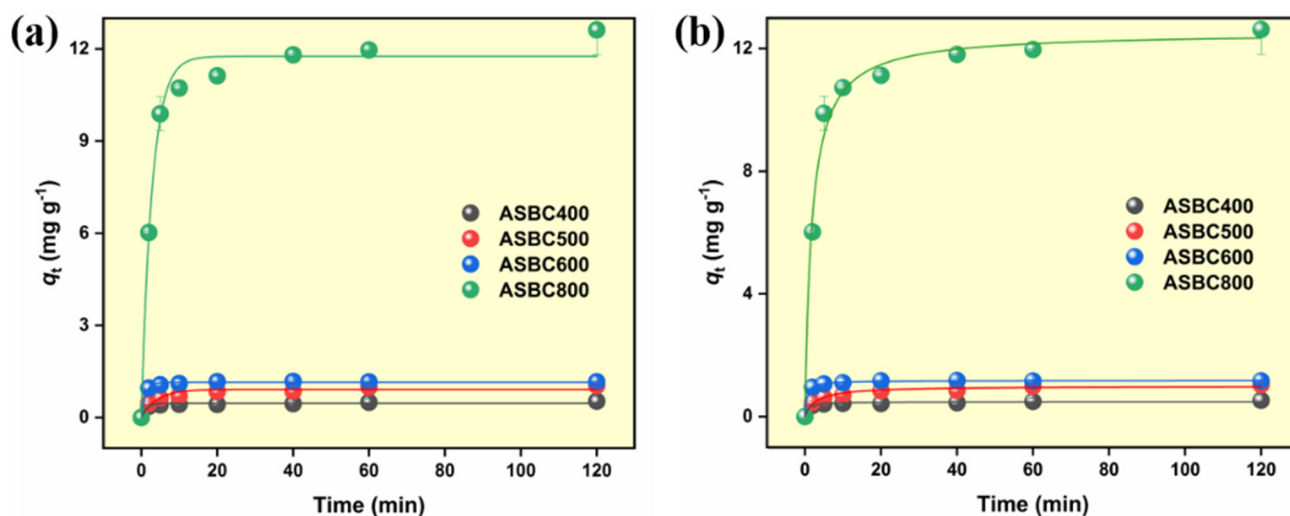


Figure 5. Pseudo-first-order (a) and pseudo-second-order (b) adsorption kinetic modelling results.

Table 2. Adsorption kinetic parameters.

Biochar	Pseudo First-Order			Pseudo Second-Order		
	q_e	k_1	R^2	q_e	k_2	R^2
ASBC400	0.461	0.721	0.941	0.482	2.696	0.967
ASBC500	0.915	0.239	0.912	0.993	0.435	0.969
ASBC600	1.144	0.881	0.991	1.175	1.816	0.999
ASBC800	11.763	0.352	0.985	12.532	0.043	0.990

3.3. Catalytic Degradation of SDZ

In order to evaluate the performance of ASBCx activated PMS, SDZ was selected as the model contaminant. As depicted in Figure S4, only 23.05% of the SDZ could be oxidized by PMS alone. For ASBC400, ASBC500 and ASBC600, negligible adsorption of SDZ was obtained (<3%), whereas ASBC800 could adsorb 37.4% of SDZ, which may be owing to the larger S_{BET} caused by higher pyrolysis temperature. As for the catalytic performance, a complete SDZ degradation removal was achieved in the ASBC800/PMS system in 40 min, while removals of 28.7%, 30.2% and 35.0% were obtained in 40 min in ASBC400/PMS, ASBC500/PMS, and ASBC600/PMS systems (Figure 6a), respectively. In addition, compared to the biochars prepared at a low temperature ($k_{obs} = 0.00425\text{--}0.00587\text{ min}^{-1}$), ASBC800 gave rise to an approximately 10-fold enhancement of reaction rate constant (0.0586 min^{-1}). As depicted in Figure 6b, a good correlation ($R^2 = 0.866$) between S_{BET} and q_e was observed, indicating that the larger S_{BET} of ASBC800 endowed it with stronger adsorptive capacity towards SDZ, and thus enhanced SDZ removal. Similarly, a good linear relationship was observed between k_{app} and q_e ($R^2 = 0.999$), suggesting that the adsorption of SDZ was beneficial for the subsequent degradation of SDZ (Figure 6c). Therefore, it could be concluded that the S_{BET} of ASBCx played a vital role both in SDZ adsorption and degradation. Notably, the ASBC800/PMS system attained a comparatively good SDZ removal rate and even surpassed some state-of-the-art metal/metal-free based oxidation systems (e.g., BC/PMS, Fe_3O_4 /PMS, Cu_2O /PMS, and MoS_2 /PMS) according to the higher SDZ normalized removal rate, faster kinetics, and lower oxidant dosage (Figure 6d).

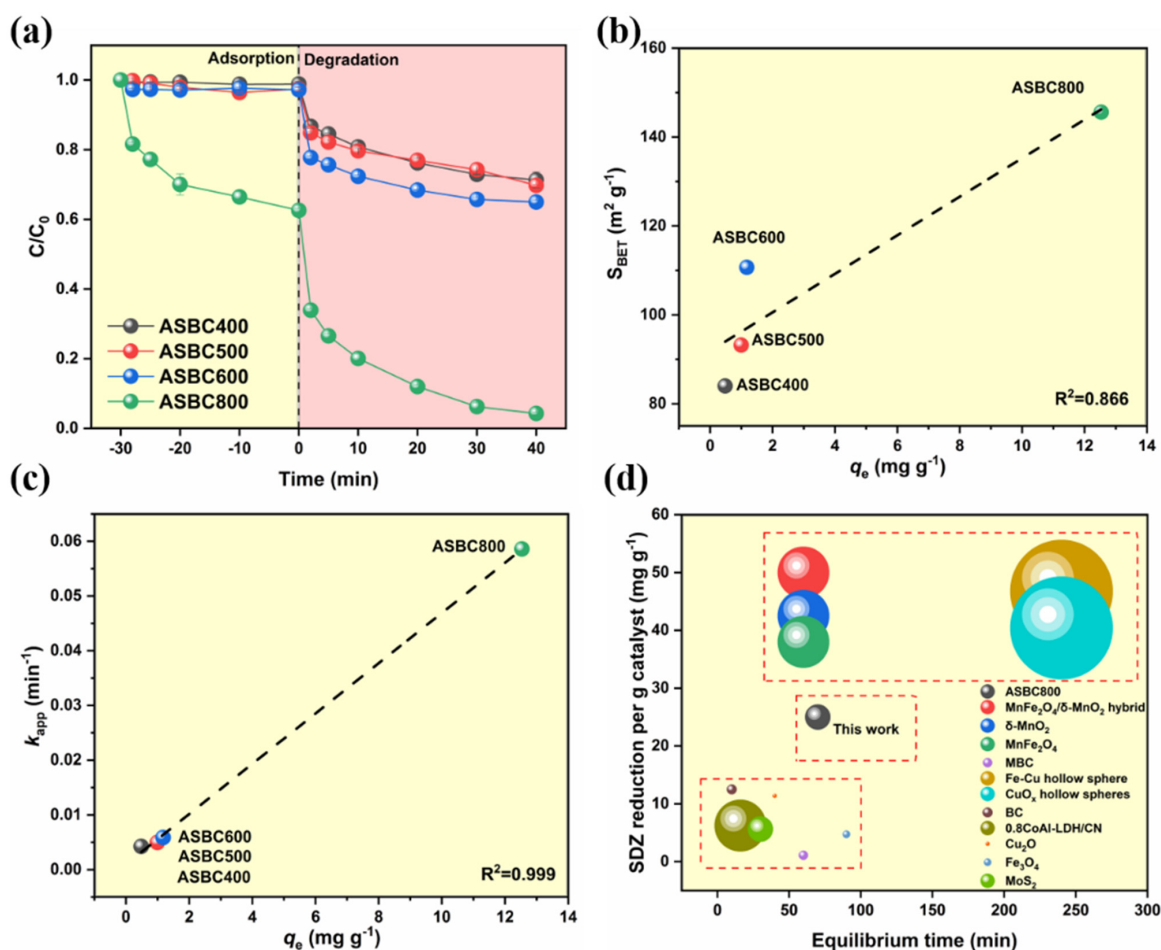


Figure 6. SDZ elimination in the PMS/ASBCx system (a), the correlation between S_{BET} and q_e (b), the correlation between k_{app} and q_e (c), and the comparisons between the ASBC800/PMS system and other PMS-based oxidation processes for SDZ removal (d). (The diameters of the balls were the ratios of PMS/SDZ).

3.4. Stability of the ASBC800/PMS System

In order to explore the practical application prospects of the ASBC800/PMS system, investigating the stability of the oxidation process was of great significance. First of all, the effect of ASBC800 dosage on SDZ degradation was explored (Figure 7a). As the ASBC800 dosage increased from 5 to 15 mg, the SDZ could be removed more quickly. This was because a higher dosage of ASBC800 could increase adsorptive sites for the PMS and SDZ, which could enhance the interaction among catalysts, oxidants and target contaminants. The effects of organic matter and inorganic anions (e.g., humic acid (HA), Cl^- , $H_2PO_4^-$) were further confirmed. HA, as a representative NOM, is often used as the model compound to explore the effects of NOM on the oxidation processes. HA with abundant electrons can function as a scavenger to consume the generated ROS, and thus obviously depress the oxidation process. More specifically, HA can attach to the surface of catalysts through π - π stacking, hydrophobic or other interactions and cover the active sites, and thus hinder the adsorption of pollutants. On the other hand, HA may compete with the target pollutants for ROS, inhibiting organic contaminants degradation. Notably, the ASBC800/PMS system could exhibit strong tolerance to HA (Figure 7b). Interestingly, Cl^- remarkably accelerated the SDZ oxidation process (Figure 7c). This was probably because Cl^- reacted with PMS, which further produced other species such as Cl^\bullet or $HOCl$, and thus synergistically degraded SDZ (Equations (1)–(11)). In addition, $H_2PO_4^-$ showed weak influences on SDZ oxidation processes (Figure 7d), which might be due to the fact that

$H_2PO_4^-$ can convert $SO_4^{\bullet-}$ and $\bullet OH$ to $HPO_4^{\bullet-}$ that have a weaker oxidizing capacity, (Equations (12) and (13)), and thus slightly suppress the oxidation process.

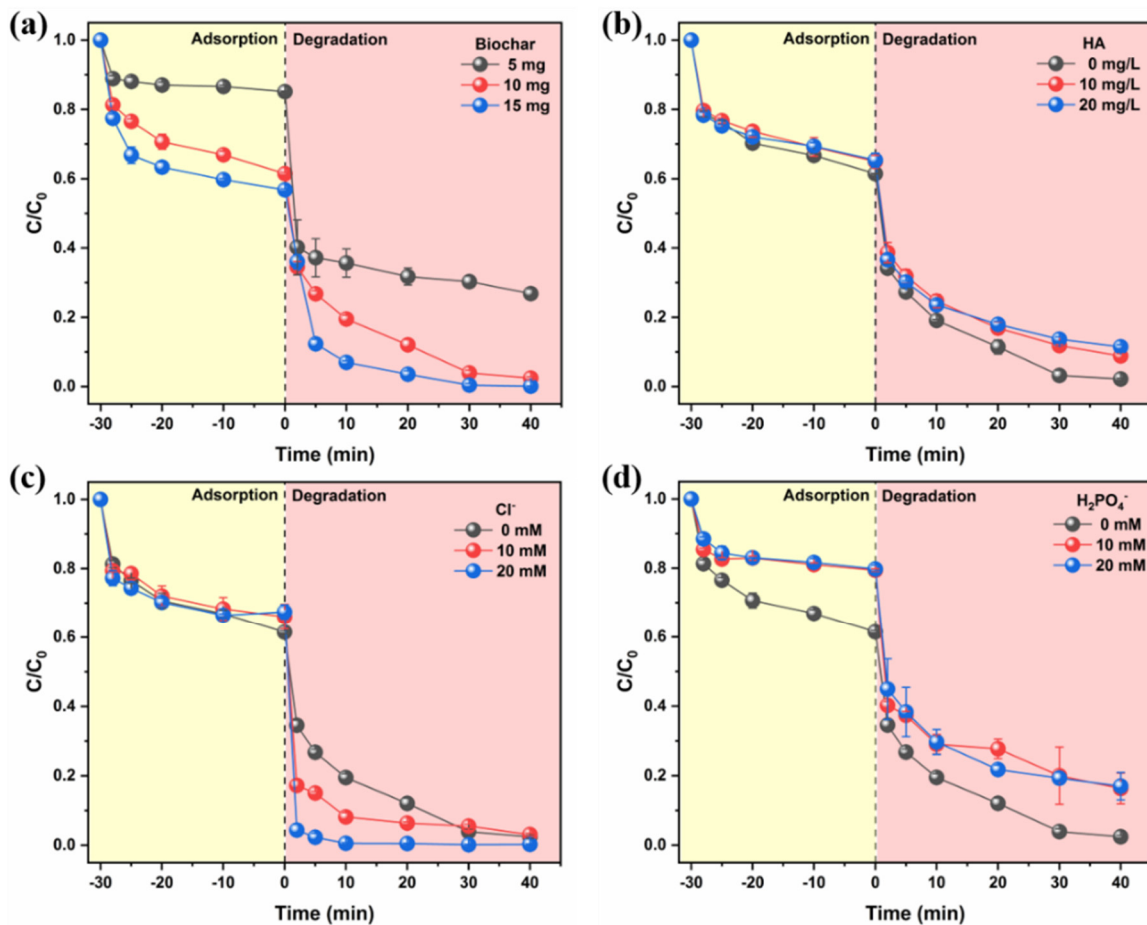
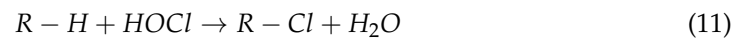
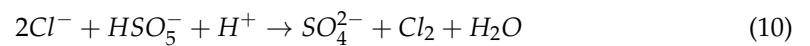
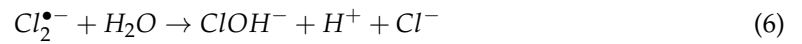


Figure 7. Effects of ASBC800 dosage (a), HA (b), Cl^- (c), $H_2PO_4^-$ (d) on SDZ removal.

3.5. Activation Mechanism

3.5.1. Identification of Reactive Oxygen Species

As evidenced in Figure 6a, the removal of SDZ was significantly boosted in the ASBC800/PMS system, suggesting the formation of reactive oxygen species (ROS). On the one hand, $\bullet\text{OH}$ and $\text{SO}_4^{\bullet-}$ could function as two primary ROS, which often dominate the radical-based oxidation process. Quenching experiments were taken firstly for elucidating the generated ROS in the ASBC800/PMS system. If radicals played vital roles in such oxidation system, the addition of methanol (MeOH) and tertiary butanol (TBA) would obviously inhibit the degradation of SDZ (Table S3). As depicted in Figure 8a, a moderate inhibition of SDZ elimination was obtained, indicating that $\bullet\text{OH}$ and $\text{SO}_4^{\bullet-}$ were produced in the ASBC800-mediated PMS activation process. Moreover, we monitored the leaching of Fe^{2+} during the oxidation process (Figure S5), and the leached Fe^{2+} content was 0.23 mg L^{-1} , which met the requirements of surface water environmental quality standards (GB3838-2002, 0.3 mg L^{-1}). In addition, the SDZ degradation experiments were also conducted in the PMS/ Fe^{2+} (0.23 mg L^{-1}) system, in which the SDZ could be removed by the homogeneous reaction system (Figure S6). Notably, both high concentrations of MeOH and TBA could not completely suppress the SDZ removal, and thus other ROS might also participate in the oxidation reaction.

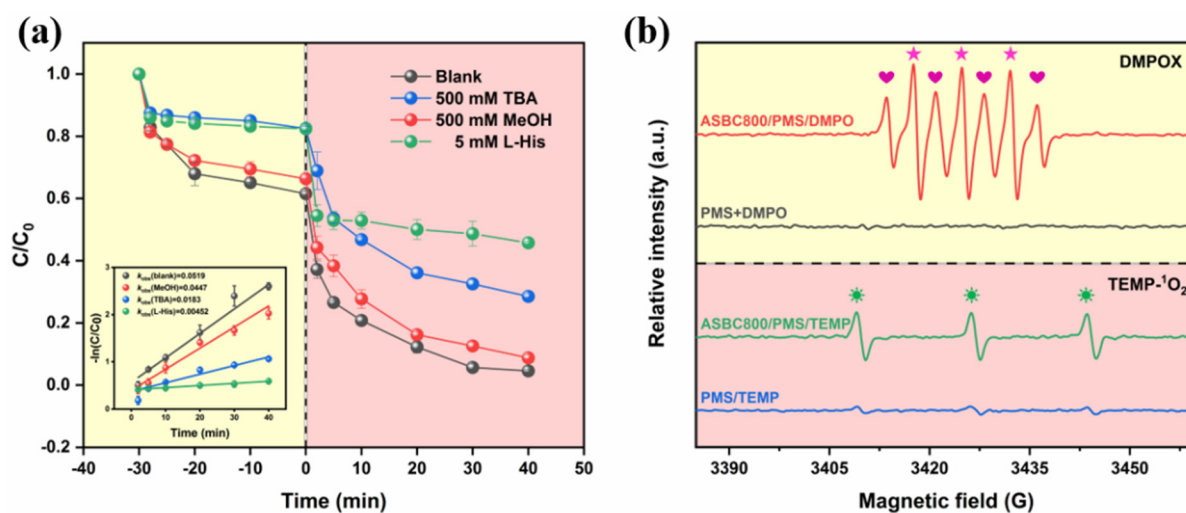


Figure 8. Effects of scavengers on SDZ degradation in PMS/ASBC800 system (a) and the result of EPR characterizations (b). (5,5-dimethylpyrroline-N-oxide: (DMPO), DMPO-adducts: (DMPOX), 2,2,6,6-tetramethyl-4-piperidinol: (TEMP), TEMP-adducts: (TEMP- $^1\text{O}_2$)).

$^1\text{O}_2$, as the selective ROS, could also oxidize contaminants, especially the electron-rich compounds. To verify the generation of $^1\text{O}_2$ in the ASBC800/PMS system, *L*-histidine (*L*-his) was chosen for the quenching experiments. As shown in Figure 8a, the oxidizing capability of the ASBC800/PMS system was effectively inhibited after adding 5 mM of *L*-his, indicating that $^1\text{O}_2$ was also generated and obligated to the elimination of SDZ. In addition, D_2O was able to accelerate the $^1\text{O}_2$ -dominated oxidation process because the lifetime of $^1\text{O}_2$ in D_2O ($55 \mu\text{s}$) was longer than that in H_2O ($4.2 \mu\text{s}$). As shown in Figure 7, SDZ removal was accelerated in D_2O , suggesting that $^1\text{O}_2$ was the contributor. The above inference could be further verified by EPR tests. As shown in Figure 8b, both DMPO-OH and DMPO- SO_4 signals were detected in the ASBC800/PMS system, and the signal of TEMP- $^1\text{O}_2$ was also observed in the ASBC800/PMS system, confirming that ASBC800 was capable of generating ROS via PMS activation.

3.5.2. Electrochemical Analysis

Apart from common reactive species produced in the oxidation system, electron-transfer regime was further investigated by electrochemical tests (Text S6). Firstly, electro-

chemical impedance spectroscopy (EIS) was measured to evaluate the conductivity of the biochars prepared under different temperatures. As depicted in Figure 9a, the semicircle diameter of ASBC800 was smallest, which suggested that ASBC800 possessed the best conductivity among other biochars and thus could serve as the favorable medium for electron transfer. Secondly, a noticeable increase in current was seen from the LSV curves with the injection of PMS (Figure 9b), demonstrating the formation of metastable ASBC800-PMS complexes (ASBC800-PMS^{*}). Notably, another remarkable increase in current was triggered upon the injection of SDZ, manifesting the formation of current flow from SDZ to ASBC800-PMS^{*}. In addition, an I-t plot was further conducted to verify this conclusion. As evidenced in Figure 9c, an obvious current jump was detected with sequential injection of PMS and SDZ, which was the solid evidence proving the occurrence of electron transfer. Overall, both radicals (e.g., $\text{SO}_4^{\bullet-}$, and $\bullet\text{OH}$), and nonradical pathways ($^1\text{O}_2$ and electron-transfer) were responsible for SDZ oxidation, in which the leached Fe^{2+} was beneficial for the generation of radicals and ASBC800 played essential roles in activating PMS, accumulating SDZ, and regulating electron shuttle from SDZ to ASBC800-PMS^{*}.

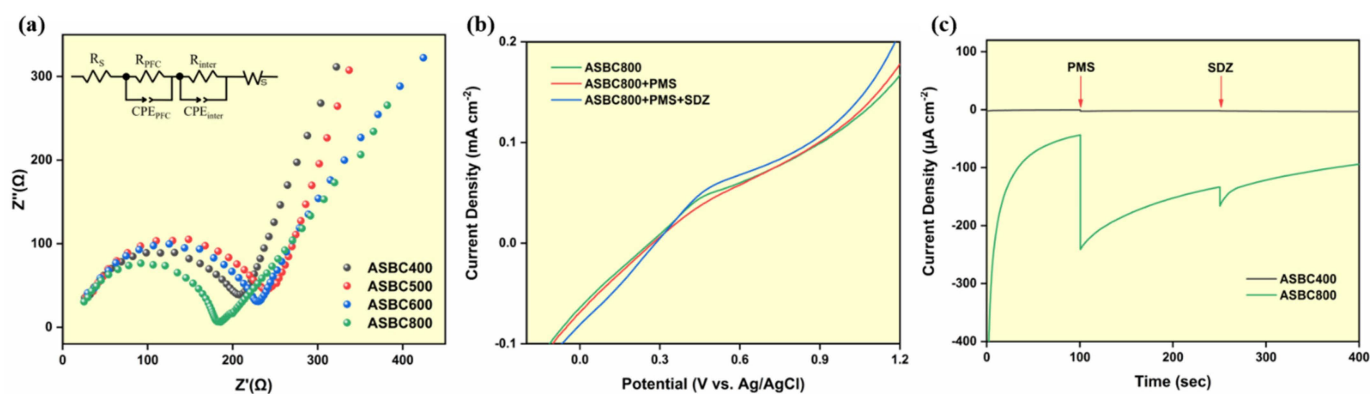


Figure 9. EIS analysis of ASBC800 (a), LSV under different conditions (b), and I-t curves (c).

3.6. Durability and Reusability

To examine the practical application potential of ASBC800 in eliminating SDZ-contaminated water, SDZ degradation experiments were performed in real river water and wastewater. As displayed in Figure 10a, unremarkable deterioration of SDZ removal was observed in river water, whereas a moderate deterioration occurred in wastewater, which might be owing to the ultra-high concentration compounds in the wastewater. Nevertheless, over 79% of SDZ was successfully degraded in river water and wastewater, indicating that ASBC800 has an excellent resistance. In addition, cycle experiments were performed to evaluate the stability of the ASBC800/PMS system. Unfortunately, we noticed a remarkable deterioration of SDZ degradation in the second run (Figure 10b). We supposed that the depletion was induced by the retarded adsorption capacity (from 38.7% of the first run to 22.75% of the second run). This was probably due to the adsorbed SDZ being not completely degraded, and thus only limited active sites could be provided for the SDZ adsorption. To verify this hypothesis, we used acetonitrile to wash the residual SDZ on the surface of ASBC800 in order to regenerate the catalyst. As expected, the adsorption efficiency of SDZ was significantly recovered from 22.75% to 28.60%, and thus the total removal rate of SDZ was also improved.

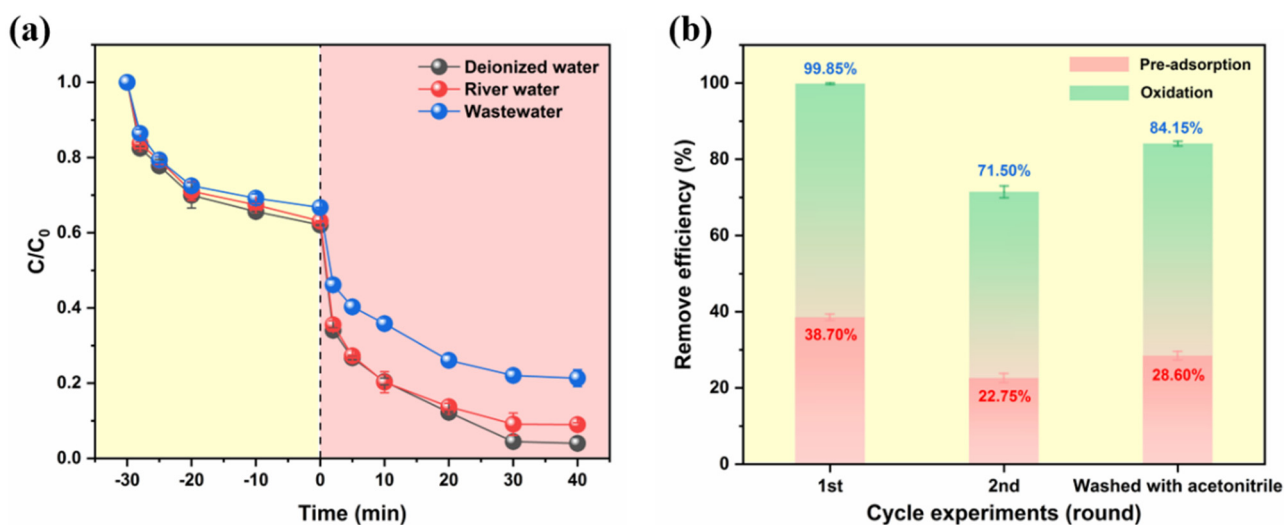


Figure 10. Elimination of SDZ in real aquatic systems (a) and the regeneration of ASBC800 (b).

4. Conclusions

In conclusion, N-rich and cost-effective biochars were fabricated by algal sludge, which were further used to catalyze PMS for SDZ degradation. To be specific, the ASBC800/PMS system exhibited excellent performance for SDZ removal (>95% within 70 min), which even surpass many state-of-the-art metal/metal-free based oxidation systems. Based on the quenching experiments, solvent exchange experiments and EPR characterizations, both radical pathways (i.e., $\cdot\text{OH}$ and $\text{SO}_4^{\cdot-}$) and nonradical pathways (i.e., $^1\text{O}_2$ and electron-transfer) were demonstrated to be responsible for SDZ removal. Notably, during the electron transfer process, PMS molecules were first adsorbed on the ASBC800 surface to form the surface-bound ASBC800-PMS* complexes, which could subsequently degrade the co-adsorbed SDZ. Owing to the selectivity of non-radical mechanisms, the ASBC800/PMS system could maintain outstanding SDZ removal efficiency even in real wastewater, indicating that ASBC800 possesses promising prospects for practical application. Overall, this study might provide a new insight into N-rich and environment friendly biochar preparation from algal sludge and deepen the insight into mechanisms of PMS activation with carbon-based functional materials.

Supplementary Materials: The following supporting information can be downloaded at: <https://www.mdpi.com/article/10.3390/coatings13020431/s1>, Figure S1: Deconvoluted C 1s XPS spectra of the ASBCx samples; Figure S2: Deconvoluted O 1s XPS spectra of the ASBCx samples; Figure S3: Deconvoluted Fe 2p XPS spectra of the ASBCx samples; Figure S4: Removal of SDZ by PMS alone; Figure S5: The leached Fe^{2+} during PMS activation; Figure S6: Removal of SDZ by PMS alone and Fe^{2+} /PMS; Figure S7: Removal of SDZ by solvent exchange experiment; Table S1: The physicochemical properties of SDZ; Table S2: Catalytic performance of reported Fenton-like catalysts for PMS activation [37–44]; Table S3: Second-order rate constants for reactions of the MeOH and TBA with different radicals; Text S1: Chemicals and reagents; Text S2: Characterizations of the biochars; Text S3: Details of electrochemical experiment; Text S4: Adsorption kinetics; Text S5: Details of degradation experiments.

Author Contributions: C.L.: writing—original draft, formal analysis, investigation, and visualization. Z.C.: writing—original draft, formal analysis, investigation, and supervision. R.K.: investigation and formal analysis. H.D.: writing—reviewing and editing, investigation. Q.L.: writing—reviewing and editing, investigation. T.W.: writing—reviewing and editing, investigation. J.W.: writing—reviewing and editing, investigation. D.T.: conceptualization, methodology. Y.X.: formal analysis, resources, writing—review and editing. Z.W.: visualization, supervision. All authors have read and agreed to the published version of the manuscript.

Funding: This work has been supported by the Research Project of Science and Technology of the Anyang City (2022C01NY016), the Research Project of Science and Technology of the Henan Province (222102320274), PhD research startup foundation of Anyang Institute of Technology (BSJ2021035), Postdoc research startup foundation of Anyang Institute of Technology (BHJ2022005), and Major science and technology projects of Anyang (201928).

Institutional Review Board Statement: All authors agreed to publish this manuscript in Environmental Science and Pollution Research.

Informed Consent Statement: All authors read and approved the final manuscript.

Data Availability Statement: The data used and/or analyzed during the current study are available from the corresponding author on reasonable request.

Conflicts of Interest: The authors declare no competing interests.

References

1. Miao, J.; Zhu, Y.; Lang, J.; Zhang, J.; Cheng, S.; Zhou, B.; Zhang, L.; Alvarez, P.; Long, M. Spin-State-Dependent Peroxymonosulfate Activation of Single-Atom M–N Moieties via a Radical-Free Pathway. *ACS Catal.* **2021**, *11*, 9569–9577. [[CrossRef](#)]
2. Xiao, C.; Hu, Y.; Li, Q.; Liu, J.; Li, X.; Shi, Y.; Chen, Y.; Cheng, J. Carbon-doped defect MoS₂ co-catalytic Fe³⁺/peroxymonosulfate process for efficient sulfadiazine degradation: Accelerating Fe³⁺/Fe²⁺ cycle and ¹O₂ dominated oxidation. *Sci. Total Environ.* **2023**, *858*, 159587. [[CrossRef](#)] [[PubMed](#)]
3. Wang, L.; Jiang, S.; Huang, J.; Jiang, H. Oxygen-doped biochar for the activation of ferrate for the highly efficient degradation of sulfadiazine with a distinct pathway. *J. Environ. Chem. Eng.* **2022**, *10*, 108537. [[CrossRef](#)]
4. Yu, J.; Feng, H.; Tang, L.; Pang, Y.; Zeng, G.; Lu, Y.; Dong, H.; Wang, J.; Liu, Y.; Feng, C.; et al. Metal-free carbon materials for persulfate-based advanced oxidation process: Microstructure, property and tailoring. *Prog. Mater. Sci.* **2020**, *111*, 100654. [[CrossRef](#)]
5. Huang, K.; Zhang, H. Direct Electron-Transfer-Based Peroxymonosulfate Activation by Iron-Doped Manganese Oxide (delta-MnO₂) and the Development of Galvanic Oxidation Processes (GOPs). *Environ. Sci. Technol.* **2019**, *53*, 12610–12620. [[CrossRef](#)] [[PubMed](#)]
6. Hu, P.; Su, H.; Chen, Z.; Yu, C.; Li, Q.; Zhou, B.; Alvarez, P.; Long, M. Selective Degradation of Organic Pollutants Using an Efficient Metal-Free Catalyst Derived from Carbonized Polypyrrole via Peroxymonosulfate Activation. *Environ. Sci. Technol.* **2017**, *51*, 11288–11296. [[CrossRef](#)] [[PubMed](#)]
7. Miao, J.; Geng, W.; Alvarez, P.; Long, M. 2D N-Doped Porous Carbon Derived from Polydopamine-Coated Graphitic Carbon Nitride for Efficient Nonradical Activation of Peroxymonosulfate. *Environ. Sci. Technol.* **2020**, *54*, 8473–8481. [[CrossRef](#)]
8. Duan, X.; Sun, H.; Wang, S. Metal-Free Carbocatalysis in Advanced Oxidation Reactions. *Acc. Chem. Res.* **2018**, *51*, 678–687. [[CrossRef](#)]
9. Cheng, X.; Li, P.; Zhou, W.; Wu, D.; Luo, C.; Liu, W.; Ren, Z.; Liang, H. Effect of peroxymonosulfate oxidation activated by powdered activated carbon for mitigating ultrafiltration membrane fouling caused by different natural organic matter fractions. *Chemosphere* **2019**, *221*, 812–823. [[CrossRef](#)]
10. Fu, C.; Sun, G.; Wang, C.; Wei, B.; Ran, G.; Song, Q. Fabrication of nitrogen-doped graphene nanosheets anchored with carbon nanotubes for the degradation of tetracycline in saline water. *Environ. Res.* **2022**, *206*, 112242. [[CrossRef](#)]
11. Huo, X.; Zhou, P.; Zhang, J.; Liu, Y.; Cheng, X.; Liu, Y.; Li, W.; Zhang, Y. N, S-Doped porous carbons for persulfate activation to remove tetracycline: Nonradical mechanism. *J. Hazard. Mater.* **2020**, *391*, 122055. [[CrossRef](#)] [[PubMed](#)]
12. Xiong, W.; Wang, Z.; He, S.; Hao, F.; Yang, Y.; Lv, Y.; Zhang, W.; Liu, P.; Luo, H. Nitrogen-doped carbon nanotubes as a highly active metal-free catalyst for nitrobenzene hydrogenation. *Appl. Catal. B Environ.* **2020**, *260*, 118105. [[CrossRef](#)]
13. Yang, B.; Kang, H.; Ko, Y.; Woo, H.; Gim, G.; Choi, J.; Kim, J.; Cho, K.; Kim, E.; Lee, S.; et al. Persulfate activation by nanodiamond-derived carbon onions: Effect of phase transformation of the inner diamond core on reaction kinetics and mechanisms. *Appl. Catal. B Environ.* **2021**, *293*, 120205. [[CrossRef](#)]
14. Ye, S.; Zeng, G.; Tan, X.; Wu, H.; Liang, J.; Song, B.; Tang, N.; Zhang, P.; Yang, Y.; Chen, Q.; et al. Nitrogen-doped biochar fiber with graphitization from *Boehmeria nivea* for promoted peroxymonosulfate activation and non-radical degradation pathways with enhancing electron transfer. *Appl. Catal. B Environ.* **2020**, *269*, 118850. [[CrossRef](#)]
15. Chen, T.; Zhou, Z.; Han, R.; Meng, R.; Wang, H.; Lu, W. Adsorption of cadmium by biochar derived from municipal sewage sludge: Impact factors and adsorption mechanism. *Chemosphere* **2015**, *134*, 286–293. [[CrossRef](#)]
16. Chen, Y.; Lin, Y.; Ho, S.; Zhou, Y.; Ren, N. Highly efficient adsorption of dyes by biochar derived from pigments-extracted macroalgae pyrolyzed at different temperature. *Bioresour. Technol.* **2018**, *259*, 104–110. [[CrossRef](#)]
17. Yu, J.; Tang, L.; Pang, Y.; Zeng, G.; Feng, H.; Zou, J.; Wang, J.; Feng, C.; Zhu, X.; Ouyang, X.; et al. Hierarchical porous biochar from shrimp shell for persulfate activation: A two-electron transfer path and key impact factors. *Appl. Catal. B Environ.* **2020**, *260*, 118160. [[CrossRef](#)]

18. Wang, H.; Guo, W.; Liu, B.; Si, Q.; Luo, H.; Zhao, Q.; Ren, N. Sludge-derived biochar as efficient persulfate activators: Sulfurization-induced electronic structure modulation and disparate nonradical mechanisms. *Appl. Catal. B Environ.* **2020**, *279*, 119361. [[CrossRef](#)]
19. Mian, M.; Liu, G.; Fu, B.; Song, Y. Facile synthesis of sludge-derived MnOx-N-biochar as an efficient catalyst for peroxymonosulfate activation. *Appl. Catal. B Environ.* **2019**, *255*, 117765. [[CrossRef](#)]
20. Zaeni, J.; Lim, W.; Wang, Z.; Ding, D.; Chua, Y.; Ng, S.; Oh, W. In situ nitrogen functionalization of biochar via one-pot synthesis for catalytic peroxymonosulfate activation: Characteristics and performance studies. *Sep. Purif. Technol.* **2020**, *241*, 116702. [[CrossRef](#)]
21. Mian, M.; Liu, G.; Zhou, H. Preparation of N-doped biochar from sewage sludge and melamine for peroxymonosulfate activation: N-functionality and catalytic mechanisms. *Sci. Total Environ.* **2020**, *744*, 140862. [[CrossRef](#)] [[PubMed](#)]
22. Zhang, P.; Yang, Y.; Duan, X.; Liu, Y.; Wang, S. Density Functional Theory Calculations for Insight into the Heterocatalyst Reactivity and Mechanism in Persulfate-Based Advanced Oxidation Reactions. *ACS Catal.* **2021**, *11*, 11129–11159. [[CrossRef](#)]
23. Wu, Q.; Zhang, Y.; Liu, H.; Liu, H.; Tao, J.; Cui, M.; Zheng, Z.; Wen, D.; Zhan, X. FeN produced in pharmaceutical sludge biochar by endogenous Fe and exogenous N doping to enhance peroxymonosulfate activation for levofloxacin degradation. *Water Res.* **2022**, *224*, 119022. [[CrossRef](#)]
24. Ren, F.; Zhu, W.; Zhao, J.; Liu, H.; Zhang, X.; Zhang, H.; Zhu, H.; Peng, Y.; Wang, B. Nitrogen-doped graphene oxide aerogel anchored with spinel CoFe₂O₄ nanoparticles for rapid degradation of tetracycline. *Sep. Purif. Technol.* **2020**, *241*, 116690. [[CrossRef](#)]
25. Ouasfi, N.; Zbair, M.; Bouzikri, S.; Anfar, Z.; Bensitel, M.; Ait Ahsaine, H.; Sabbar, E.; Khamliche, L. Selected pharmaceuticals removal using algae derived porous carbon: Experimental, modeling and DFT theoretical insights. *RSC Adv.* **2019**, *9*, 9792–9808. [[CrossRef](#)] [[PubMed](#)]
26. Ji, R.; Wu, Y.; Bian, Y.; Song, Y.; Sun, Q.; Jiang, X.; Zhang, L.; Han, J.; Cheng, H. Nitrogen-doped porous biochar derived from marine algae for efficient solid-phase microextraction of chlorobenzenes from aqueous solution. *J. Hazard. Mater.* **2021**, *407*, 124785. [[CrossRef](#)] [[PubMed](#)]
27. Wang, H.; Wang, H.; Zhao, H.; Yan, Q. Adsorption and Fenton-like removal of chelated nickel from Zn-Ni alloy electroplating wastewater using activated biochar composite derived from Taihu blue algae. *Chem. Eng. J.* **2020**, *379*, 122372. [[CrossRef](#)]
28. Wang, H.; Wang, H.; Liu, G.; Yan, Q. In-situ pyrolysis of Taihu blue algae biomass as appealing porous carbon adsorbent for CO₂ capture: Role of the intrinsic N. *Sci. Total Environ.* **2021**, *771*, 145424. [[CrossRef](#)]
29. Gaballah, M.; Guo, J.; Hassanein, A.; Sobhi, M.; Zheng, Y.; Philibert, M.; Li, B.; Sun, H.; Dong, R. Removal performance and inhibitory effects of combined tetracycline, oxytetracycline, sulfadiazine, and norfloxacin on anaerobic digestion process treating swine manure. *Sci. Total Environ.* **2023**, *857*, 159536. [[CrossRef](#)]
30. Yu, J.; Tang, L.; Pang, Y.; Zeng, G.; Wang, J.; Deng, Y.; Liu, Y.; Feng, H.; Chen, S.; Ren, X. Magnetic nitrogen-doped sludge-derived biochar catalysts for persulfate activation: Internal electron transfer mechanism. *Chem. Eng. J.* **2019**, *364*, 146–159. [[CrossRef](#)]
31. Zhong, K.; Li, M.; Yang, Y.; Zhang, H.; Zhang, B.; Tang, J.; Yan, J.; Su, M.; Yang, Z. Nitrogen-doped biochar derived from watermelon rind as oxygen reduction catalyst in air cathode microbial fuel cells. *Appl. Energ.* **2019**, *242*, 516–525. [[CrossRef](#)]
32. Zhu, K.; Bin, Q.; Shen, Y.; Huang, J.; He, D.; Chen, W. In-situ formed N-doped bamboo-like carbon nanotubes encapsulated with Fe nanoparticles supported by biochar as highly efficient catalyst for activation of persulfate (PS) toward degradation of organic pollutants. *Chem. Eng. J.* **2020**, *402*, 126090. [[CrossRef](#)]
33. Li, X.; Jia, Y.; Zhou, M.; Su, X.; Sun, J. High-efficiency degradation of organic pollutants with Fe, N co-doped biochar catalysts via persulfate activation. *J. Hazard. Mater.* **2020**, *397*, 122764. [[CrossRef](#)] [[PubMed](#)]
34. Cheng, X.; Dou, S.; Qin, G.; Wang, B.; Yan, P.; Isimjan, T.; Yang, X. Rational design of highly selective nitrogen-doped Fe₂O₃-CNTs catalyst towards H₂O₂ generation in alkaline media. *Int. J. Hydrogen Energ.* **2020**, *45*, 6128–6137. [[CrossRef](#)]
35. Qi, Y.; Ge, B.; Zhang, Y.; Jiang, B.; Wang, C.; Akram, M.; Xu, X. Three-dimensional porous graphene-like biochar derived from Enteromorpha as a persulfate activator for sulfamethoxazole degradation: Role of graphitic N and radicals transformation. *J. Hazard. Mater.* **2020**, *399*, 123039. [[CrossRef](#)]
36. Ho, S.; Chen, Y.; Li, R.; Zhang, C.; Ge, Y.; Cao, G.; Ma, M.; Duan, X.; Wang, S.; Ren, N. N-doped graphitic biochars from C-phycocyanin extracted Spirulina residue for catalytic persulfate activation toward nonradical disinfection and organic oxidation. *Water Res.* **2019**, *159*, 77–86. [[CrossRef](#)]
37. Dong, F.; Yan, L.; Huang, S.; Liang, J.; Zhang, W.; Yao, X.; Chen, X.; Qian, W.; Guo, P.; Kong, L.; et al. Removal of antibiotics sulfadiazine by a biochar based material activated persulfate oxidation system: Performance, products and mechanism. *Process Saf. Environ.* **2021**, *157*, 411–419. [[CrossRef](#)]
38. Feng, Y.; Wu, D.; Deng, Y.; Zhang, T.; Shih, K. Sulfate Radical-Mediated Degradation of Sulfadiazine by CuFeO₂ Rhombohedral Crystal-Catalyzed Peroxymonosulfate: Synergistic Effects and Mechanisms. *Environ. Sci. Technol.* **2016**, *50*, 3119–3127. [[CrossRef](#)]
39. Jiang, Z.; Li, Y.; Zhou, Y.; Liu, X.; Wang, C.; Lan, Y.; Li, Y. Co₃O₄-MnO₂ nanoparticles moored on biochar as a catalyst for activation of peroxymonosulfate to efficiently degrade sulfonamide antibiotics. *Sep. Purif. Technol.* **2021**, *281*, 119935. [[CrossRef](#)]
40. Li, Y.; Feng, Y.; Yang, B.; Yang, Z.; Shih, K. Activation of peroxymonosulfate by molybdenum disulfide-mediated traces of Fe(III) for sulfadiazine degradation. *Chemosphere* **2021**, *283*, 131212. [[CrossRef](#)]
41. Liu, T.; Wu, K.; Wang, M.; Jing, C.; Chen, Y.; Yang, S.; Jin, P. Performance and mechanisms of sulfadiazine removal using persulfate activated by Fe₃O₄@CuOx hollow spheres. *Chemosphere* **2021**, *262*, 127845. [[CrossRef](#)] [[PubMed](#)]

42. Tan, C.; Lu, X.; Cui, X.; Jian, X.; Hu, Z.; Dong, Y.; Liu, X.; Huang, J.; Deng, L. Novel activation of peroxymonosulfate by an easily recyclable VC@Fe₃O₄ nanoparticles for enhanced degradation of sulfadiazine. *Chem. Eng. J.* **2019**, *363*, 318–328. [[CrossRef](#)]
43. Zeng, H.; Zhang, H.; Deng, L.; Shi, Z. Peroxymonosulfate-assisted photocatalytic degradation of sulfadiazine using self-assembled multi-layered CoAl-LDH/g-C₃N₄ heterostructures: Performance, mechanism and eco-toxicity evaluation. *J. Water Process Eng.* **2019**, *33*, 101084. [[CrossRef](#)]
44. Zhu, L.; Shi, Z.; Deng, L.; Duan, Y. Efficient degradation of sulfadiazine using magnetically recoverable MnFe₂O₄/δ-MnO₂ hybrid as a heterogeneous catalyst of peroxymonosulfate. *Colloid Surface A* **2021**, *609*, 125637. [[CrossRef](#)]

Disclaimer/Publisher's Note: The statements, opinions and data contained in all publications are solely those of the individual author(s) and contributor(s) and not of MDPI and/or the editor(s). MDPI and/or the editor(s) disclaim responsibility for any injury to people or property resulting from any ideas, methods, instructions or products referred to in the content.